Monthly Notices
of the
ROYAL ASTRONOMICAL SOCIETY

MNRAS **473,** 148–164 (2018)
Advance Access publication 2017 August 31

doi:10.1093/mnras/stx2190

The first optical spectra of Wolf–Rayet stars in M101 revealed with Gemini/GMOS

J. L. Pledger,[1⋆] M. M. Shara,[2] M. Wilde,[2] P. A. Crowther,[3] K. S. Long,[4] D. Zurek[2] and A. F. J. Moffat[5]

[1]*Jeremiah Horrocks Institute for Mathematics, Physics and Astronomy, University of Central Lancashire, Preston PR1 2HE, UK*
[2]*Department of Astrophysics, American Museum of Natural History, Central Park West and 79th Street, New York, NY 10024-5192, USA*
[3]*Department of Physics and Astronomy, University of Sheffield, Hounsfield Road, Sheffield S3 7RH, UK*
[4]*Space Telescope Science Insitute, 3700 San Martin Drive, Baltimore, MD 21218, USA*
[5]*Département de Physique, Université de Montréal, CP 6128 Succ. C-V, Montréal, QC H3C 3J7, Canada*

Accepted 2017 August 21. Received 2017 August 21; in original form 2017 April 5

ABSTRACT

Deep narrow-band *Hubble Space Telescope* (*HST*) imaging of the iconic spiral galaxy M101 has revealed over a thousand new Wolf–Rayet (WR) candidates. We report spectrographic confirmation of 10 He II-emission line sources hosting 15 WR stars. We find WR stars present at both sub- and super-solar metallicities with WC stars favouring more metal-rich regions compared to WN stars. We investigate the association of WR stars with H II regions using archival *HST* imaging and conclude that the majority of WR stars are in or associated with H II regions. Of the 10 emission lines sources, only one appears to be unassociated with a star-forming region. Our spectroscopic survey provides confidence that our narrow-band photometric candidates are in fact bona fide WR stars, which will allow us to characterize the progenitors of any core-collapse supernovae that erupt in the future in M101.

Key words: techniques: imaging spectroscopy – Stars: Wolf-Rayet – H II regions – galaxies: stellar content.

1 INTRODUCTION

Wolf–Rayet (WR) stars are the descendants of massive O stars. They display powerful stellar winds, resulting in unique, broad emission-line spectra that allow us to detect WR stars in both the Local Group (Moffat & Shara 1983; Massey & Johnson 1998; Neugent & Massey 2011) and more distant star-forming galaxies (Conti & Vacca 1990; Hadfield et al. 2005). The strong stellar winds strip the outer layers, revealing the nuclear by-products of central core burning in the photosphere of the star. The products of hydrogen burning via the CNO cycle are seen at the surface in nitrogen-rich WN stars, while the products of helium burning are revealed in more evolved carbon-rich WC stars and even more evolved oxygen-rich WO stars.

Stellar evolutionary theory suggests that massive stars end their lives as core-collapse supernovae (ccSNe), providing chemical enrichment within the interstellar medium. Indeed, Red Supergiants (RSGs) between 8 and 16 $M_{\odot}$ have been directly observed to produce hydrogen-rich Type II-P ccSNe (Smartt 2009; Maund et al. 2014). Theoretical models have also supported WN and WC stars as progenitors of H-poor Type Ib and H- and He-poor Type Ic ccSNe, respectively, since such elements have been stripped from the star via strong stellar winds (Groh, Georgy & Ekström 2013).

Since most O and WR stars are in massive binaries, one expects the ccSN of the initially more massive star to lead to a Black Hole (BH) + O star, followed by a BH+WR star binary. Examples of such systems include Cyg X-1 (Gies et al. 2003) as well as IC10 X-1 (Prestwich et al. 2007; Silverman & Filippenko 2008), NGC300 X-1 (Crowther et al. 2010) and M33 X-7 (Orosz et al. 2007). However, such systems are rare and normally the asymmetric SN explosion combined with the orbital motion in the original binary will lead to two runaway stars, one of which will evolve as a single WR star.

One problem with this massive star evolution scenario is the growing lack of direct detections of Type Ib/c progenitors, which has called into question the WR–ccSNe connection (Smartt 2009). For example, pre-explosion images at the location of Type Ic SN 2002ap in M74 failed to reveal a progenitor down to $M_B = -4.2$ mag. A binary scenario was, instead, favoured by Crockett et al. (2007). In addition, Eldridge et al. (2013) suggest that *all* Type Ib/c progenitors are the result of low-mass helium cores produced during binary evolution, proposing that the WR stars may produce BHs with which no visible component is associated. However, Smith et al. (2011) show that the inclusion of both binary and single evolutionary paths is optimum for reproducing the observed ccSNe rate from a standard initial mass function whilst Cao et al. (2013) report that the

⋆ E-mail: jpledger@uclan.ac.uk

© 2017 The Authors
Published by Oxford University Press on behalf of the Royal Astronomical Society

Downloaded from https://academic.oup.com/mnras/article-abstract/473/1/148/4101236
by University of Central Lancashire user
on 02 November 2017

photometric properties of the progenitor of Type Ib SN iPTF13bvn are consistent with those of a WR star. Similarly, analysis of the light curve and ejecta mass of the Type Ibn SN OGLE-2014-SN-131 suggests a massive WR progenitor, although no direct detection has been made (Karamehmetoglu et al. 2017).

We need a catalogue of ∼20 000 WR stars to definitively demonstrate that WR stars are, or are not, the progenitors of Type Ibc SNe. This is because the mean lifetime of a WR star is ∼300 000 yr so assuming that each star has an average of ∼150 000 yr left as a WR star, one WR star from a sample of 20 000 should explode as a Type Ibc SN within 7 yr, although one within 50 yr would be a more conservative estimate. Conversely, the demonstration that Type Ibc SNe come from objects that are fainter in He II than the faintest known WR stars, such as those in the metal-poor Small Magellanic Cloud, would indicate that most WR stars do not end their lives as SNe.

M101 is an ideal galaxy with which to study the content and associated environments of WR stars. At a distance of 6.4 Mpc (Shappee & Stanek 2011), we are still able to resolve large clusters, and the face-on orientation is favourable to an acceptable level of extinction, typically between 0.25–1 mag (Cedrés & Cepa 2002). Based on Hα imaging, Kennicutt (1998) determined a star formation rate (SFR) $\sim 1.7\,M_\odot\,yr^{-1}$. This is a lower limit as they note that coverage is not complete, which is consistent with the upper value of SFR $\sim 3.3\,M_\odot\,yr^{-1}$ found by Jarrett et al. (2013) from ultraviolet and infrared observations. Based on a Milky Way SFR $\sim 2\,M_\odot\,yr^{-1}$ (Chomiuk & Povich 2011) and a predicted Galactic WR population ∼1900 (Rosslowe & Crowther 2015), we expect ∼3000 WR stars in M101.

In addition, M101 has a strong metallicity gradient, extending from a supersolar metallicity of log(O/H)+12 = +8.9 in the central regions to log(O/H)+12 = +7.5 in the outer regions (Rosa & Benvenuti 1994; Bresolin 2007; Cedrés, Urbaneja & Cepa 2004), allowing us to test N(WR)/N(O) and N(WN)/N(WC) ratios, as a function of ambient metallicity predicted from stellar evolutionary models (Eldridge & Vink 2006; Meynet & Maeder 2005).

Currently the only published spectrum of a WR star in M101 is that of the WR counterpart to ULX-1, which is identified as a WN8 star by Liu et al. (2013). In this paper, we present new Gemini/GMOS spectroscopy of 10 WR candidates identified from *F*469*N* narrow-band imaging using WFC3 on *HST*. In Section 2, we describe details of our observations, followed by our data reduction techniques in Section 3. Our results are presented in Section 4, along with Hα analysis in Section 5. Discussion of our non-detections is presented in Section 4.4 followed by a summary in Section 6.

2 OBSERVATIONS

M101 was observed in Cycle 17 by the *HST* Wide Field Camera 3 (*HST*/WFC3), under program ID 11635 (PI. Shara). Eighteen pointings, each with a 2.7 × 2.7 arcmin^2 field of view, were obtained using the narrow-band *F469N* filter (tuned to He II λ4684 Å) to identify WR candidates. A detailed account of the image analysis and first results is presented in Shara et al. (2013). At a distance of 6.4 Mpc (Shappee & Stanek 2011), our M101 imaging has a spatial scale of ∼1.24 pc pixel^{-1} based on *HST*/WFC3 0.04 arcsec pixel^{-1}.

Full details of our imaging survey and initial results are presented in Shara et al. (2013). In summary, we found 25 *F*469*N* bright objects as WR candidates and 71 candidate RSG stars in one of our 18 *HST* fields. We noted their distribution, namely that the WR stars were much more concentrated in the young star-forming complex NGC 5462 compared to the RSG. This is all predicated on the assumption that the *F*469*N* bright objects *really* are WR stars. This demands follow-up spectroscopy of the WR candidates, which will also allow us to distinguish between WN and WC stars. This is also a test of stellar evolutionary theory that predicts more WC stars in metal-rich regions of the galaxy.

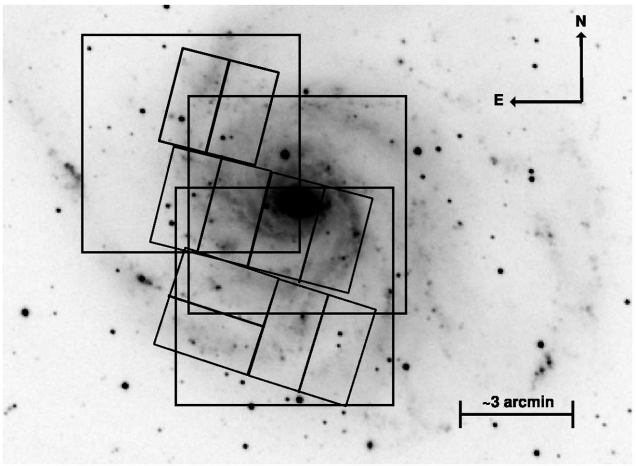

Figure 1. An image of M101 taken with the KPNO Schmidt telescope trimmed to ∼16.5 × 12 arcmin^2 showing the location of the three GMOS pointings, each of 5.5 × 5.5 arcmin^2 and the corresponding WFC3 pointings of 2.7 × 2.7 arcmin^2.

As a first step, we obtained observations with the Gemini-North Multi-Object Spectrograph (GMOS) under program ID GN-2012A-Q-49 (PI: Bibby). In total, seven GMOS masks were designed, providing good coverage of the central region of M101. By observing additional spectrophotometric standard stars we were also able to flux calibrate the spectra to ascertain whether each WR candidate is in fact multiple WR stars, as is commonly seen in previous studies e.g. in NGC 2403 (Drissen et al. 1999) and NGC 7793 (Bibby & Crowther 2010).

2.1 Pre-imaging

The 5 × 5 arcmin^2 GMOS field is approximately twice the size of the *HST*/WFC3 field of view and as such each GMOS pointing covers several *HST* pointings. To design the MOS masks from the WFC3/*F*469*N* imaging would have required multiple pointings to be combined on to a single mosaic image. Unfortunately, this was not possible as the *F*469*N* fields did not overlap sufficiently. Consequently, we opted to use GMOS imaging to ensure that we could take full advantage of the ∼30 slits GMOS can accommodate.

The Gemini Science Archive contained *g*-band imaging obtained on 2007 February 21, under program ID GN-2007A-Q-72 (PI: Chandar), which covered the central and north-east regions of M101. However, in order to sample the complete radial distribution of WR stars we obtained additional pre-imaging on 2012 February 16, covering the southern central region of M101. The coverage of M101 with both *HST* and Gemini is shown in Fig. 1. The archival and new GMOS imaging had similar spatial resolutions of ∼1.0 and ∼1.1 arcsec, respectively.

2.2 GMOS spectroscopy

GMOS of WR candidates in M101 was obtained during 2012 April–June in seeing conditions ranging between ∼0.7 and ∼1.0 arcsec. The R150 grism was used, with no blocking filter, to allow a large

Downloaded from https://academic.oup.com/mnras/article-abstract/473/1/148/4101236
by University of Central Lancashire user
on 02 November 2017

Table 1. Observational log for Gemini/GMOS observations of M101 obtained under program ID GN-2012A-Q49 (PI: Bibby). The number in parenthesis indicates the number of exposures obtained.

Date	MOS mask	Exposure time (s)	λ_c (Å)	Airmass	Seeing (arcsec)
2012 Feburary 28	#1	2240 (2)	510	1.28	0.75
2012 Feburary 28	#1	2240 (2)	530	1.22	0.87
2012 April 3	#2	2240 (2)	510	1.30	0.73
2012 April 12	#2	2240 (2)	530	1.43	0.73
2012 April 13	#3	2240 (2)	510	1.29	0.93
2012 April 26	#3	2240 (2)	530	1.24	0.73
2012 April 26	#4	2300 (3)	510	1.25	0.73
2012 May 20	#4	2300 (2)	530	1.34	0.71
2012 May 21	#4	2300 (1)	530	1.34	0.80
2012 May 21	#5	2240 (2)	510	1.22	0.80
2012 May 21	#5	2240 (1)	530	1.23	0.80
2012 June 29	#5	2240 (1)	530	1.26	0.79
2012 June 27	#6	2240 (2)	510	1.29	0.59
2012 June 29	#6	2240 (1)	530	1.22	0.79
2012 June 29	#7	2240 (2)	510	1.36	0.79
2012 June 30	#7	2240 (2)	530	1.23	0.75

wavelength range to include numerous stellar and nebular diagnostic lines. Standard dithering techniques were used with a central wavelength of 510 and 530 nm to provide full coverage across the chip gaps on GMOS in the spectral dimension.

MOS masks were designed using the Gemini mask preparation software and co-ordinates were transformed from *HST*/WFC3 imaging to Gemini pre-imaging. Any gaps in the MOS mask design were filled with slits placed on H II regions to maximize the science output; results of these regions will be presented in a future paper.

The spectral dispersion obtained $\sim$3.5 Å pixel^{-1} and the resolution was derived from nebular lines to be $\sim$15 Å. Exposure times for MOS masks #1–3 and # 5–7 were 4 $\times$ 2240 s, while MOS mask #4 was observed for 6 $\times$ 2300 s as we tried to sample the faintest WR candidates, at the limit of GMOS's capability. A summary of the spectroscopic observations is presented in Table 1.

3 DATA REDUCTION AND CALIBRATION

Spectroscopic data reduction was performed using standard Gemini IRAF[1] reduction packages including GPREPARE and GSREDUCE. Wavelength calibration was performed from observations of a CuAr lamp using the same instrumental setup and MOS mask as the science observations.

In order for flux calibration to be possible, we obtained observations of the spectrophotometric standard HZ44 (Oke 1990) on the same night as MOS mask #1. The second-order contamination from the R150 grism prevented the Gemini IRAF software from being used so flux calibration was achieved using the STARLINK package FIGARO instead (Shortridge et al. 2004). The wavelength range was trimmed to 4000–7000 Å to remove the majority of the second-order contamination and both the observed and tabulated standards were fitted with a spline function and then divided by each other to produce a calibration curve.

Since our observing program only allowed for one standard star observation, we cross-calibrated the other MOS masks using a common object and determining a calibration factor. The exception was MOS mask #6 and #7, which covered the most southerly region of M101 and which did not contain the calibration object so an additional object was used. Unfortunately, this object was too faint to extract with the Gemini packages so cross-calibration could not be performed in this way; however, the calibration factor for the other MOS masks were relatively consistent so the average was used.

To achieve an absolute flux calibration, we have to account for slit losses since not all of the WR light will enter the slit. This was achieved by comparing the empirical photometric magnitude of each source to its spectroscopic magnitude calculated by convolving the observed spectrum with the filter bandpass. For masks #1,2,5 and 6, we found the fraction of light in the slit to be 0.86, and 0.76 for mask #4. No WR sources were extracted from mask #7 so no slit losses were determined. The majority of the synthetic magnitudes revealed a brighter source than in the *HST* imaging, suggesting that the spectra were contaminated by additional sources. This is not surprising or unexpected since the GMOS slit width is significantly larger than the *HST*/WFC3 resolution.

4 RESULTS

The GMOS spectra were analysed using the emission line fitting (ELF) routine within DIPSO to measure line fluxes of both stellar and nebular emission lines (Howarth et al. 2004).

4.1 Nebular analysis

Where possible we made local estimates of extinction using Balmer line ratios, assuming Case B recombination for an optically thick nebula and a Standard Galactic Extinction Law. We used the Hα/Hβ = 2.86 line ratio for all nebular sources apart from #48 and #112, where the Hβ line unfortunately fell within the chip gap due to the source being unable to be extracted in one or more of the exposures. In both cases, the H$\gamma\lambda$4343 emission line was present so we used the Hα/Hγ = 0.164 line ratio (Osterbrock & Ferland, 2006) to determine extinction. The line fluxes and resulting $E(B-V)$ values for each nebular source are presented in Table 2. We note that where there were no nebular lines present, we adopt a value of $E(B-V) = 0.44$ mag from Lee et al. (2009), which is consistent with our average of $E(B-V) = 0.42 \pm 0.07$ mag.

For estimates of the metallicity of the nebular regions, we rely on the strong line method of Pettini & Pagel (2004) using the [N II]/Hα ratio as a proxy for metallicity since the [O II]λ3727 line was not detected in our spectra. Given the proximity of [N II] λ6583 to the Hα λ6568 emission line, the narrow-band filter includes a contribution from both, and hence we need to correct for this contribution in our measurement of L(Hα). Where nebular lines are present in our GMOS spectra the [N II]/Hα ratio has been determined directly whilst for others a ratio of [N II]/Hα = 0.54 has been taken from Kennicutt et al. (2008). This is slightly higher than our average [N II]/Hα ratio of 0.37 $\pm$ 0.07 albeit from a small sample size.

Using the N2 method from Pettini & Pagel (2004) to determine the metallicity of those H II regions hosting WR stars, we find a range of log(O/H)+12 = 8.41–8.80 with errors of $\pm$0.4 dex. Using the O3N2 indicator, we find a similar range of log(O/H)+12 = 8.56–8.92 ($\pm$0.25 dex) with regions in general agreement by $\pm$0.15 dex. The derived metallicity for Source #1024 differs by $\sim$0.3 dex between methods but is still in agreement within errors. Overall, we find an average value of log(O/H)+12 = 8.66 $\pm$ 0.24 dex for the metallicity of H II regions in M101. This is consistent with the metallicities derived in Bresolin (2007) and Rosa & Benvenuti (1994) but

[1] IRAF is distributed by the National Optical Astronomy Observatories, which are operated by the Association of Universities for Research in Astronomy, Inc., under cooperative agreement with the National Science Foundation.

Downloaded from https://academic.oup.com/mnras/article-abstract/473/1/148/4101236
by University of Central Lancashire user
on 02 November 2017

Table 2. Nebular analysis of H II regions hosting WR stars. Fluxes and Intensities are given relative to H $\alpha = 100$, where Hα is in units of $\times 10^{-16}$ erg s^{-1} cm^{-2} and extinctions are determined using Balmer line ratios of H α/H $\beta = 2.86$ or H γ/H $\alpha = 0.165$ (Osterbrock & Ferland, 2006). The metallicity of the region is determined using both the N2 and O3N2 methods of Pilyugin & Thuan (2005). c/g indicates that the line was in the chip gap so no flux was measured.

		Source ID						
ID	λ(Å)	48	1012	1016	49	112	1024	2053
F(H δ)	4100	7.71	–	–	–	–	–	–
I(H δ)	4100	9.67	–	–	–	–	–	–
F(H γ)	4343	13.3	16.5	6.47	–	7.19	10.9	5.57
I(H γ)	4343	16.3	18.8	17.9	–	15.9	21.7	24.0
F(H β)	4861	c/g	32.0	19.0	30.8	c/g	21.7	12.7
I(H β)	4861	c/g	35.1	35.2	33.9	c/g	35.3	9.03
F([O III])	4959	22.1	–	–	9.74	3.03	0.37	6.73
I([O III])	4959	25.5	–	–	10.4	5.07	0.51	21.2
F([O III])	5007	53.8	1.68	3.96	49.5	8.94	2.80	7.71
I([O III])	5007	61.7	1.59	7.16	54.7	14.8	4.21	23.1
F(H α)	6563	100	100	100	100	100	100	100
I(H α)	6563	100	100	100	100	100	100	100
F([N II])	6583	31.2	34.8	64.6	66.6	30.0	22.6	14.7
I([N II])	6583	31.2	34.7	63.3	66.7	29.9	22.5	14.2
F(H α)	6563	42.0	71.3	236.6	3.80	143.2	66.7	224.3
I(H α)	6563	57.7	86.5	929.1	4.98	475.7	189.4	2058.0
$E(B-V)$		0.14	0.09	0.59	0.12	0.53	0.46	0.98
**[N II]/H α		0.31	0.35	0.63	0.67	0.30	0.22	0.14
log(O/H)+12[a]		8.61	8.64	8.79	8.80	8.60	8.53	8.41
O III/H β		–	0.40	0.20	1.61	–	0.12	0.60
log(O/H)+12[b]		–	8.74	8.92	8.64	–	8.85	8.56
log(O/H)+12[c]		8.61	8.69	8.85	8.72	8.60	8.69	8.49
R/R_{25}		0.18	0.11	0.13	0.16	0.16	0.08	0.22
log(O/H)+12[d]		8.60	8.66	8.64	8.62	8.62	8.67	8.56

Notes. [a]From N2; [b]from O3N2; [c]mean log(O/H)+12; and [d]log(O/H)+12 based on the gradient in Cedrés et al. (2004).

is slightly higher than we would expect from the metallicity gradient of 8.769(±0.06)–0.90(±0.08)(R/R$_0$) found by Cedrés et al. (2004). One explanation may be that all of our regions lie within the central regions of M101 with R/R_{25} of 0.04 to 0.22, based on an inclination of 18°, PA = 45°(Kenney & Lord 1991) and a distance of 6.4 Mpc. In contrast, the majority of the 90 regions used by Cedrés et al. (2004) are within R/R$_0$ = 0.30.

4.2 Stellar analysis

WR candidates can be identified from narrow-band He II imaging and photometry but they can only be confirmed as bona fide WR stars from spectroscopy. The photometric properties of each WR candidate presented in this paper are taken from *HST* imaging (see Shara et al. (2013) for details) and are presented in Table 3. Spectroscopy allows us to identify Nitrogen-rich (WN) stars predominantly from their He II λ4686 emission line, while carbon-rich (WC) stars are seen to be dominated by C III λ4650 and C IV λ5808. Rarer oxygen-rich (WO) stars are identified by O IV λ3811-34 emission lines; however, these lines lie outside the spectral range of our observations.

We have spectroscopically confirmed 10 WR sources within M101, as indicated in Fig. 2. For completeness, we present more detailed finding charts in Appendix B. As for the nebular analysis, we used the DIPSO ELF routine to measure the flux from the stellar source, results of which are presented in Table 4. Typical errors for the flux measurements were higher than expected at ∼±20 per cent for strong lines such as He II and C IV. This is likely due to the fact that the 1 arcsec slit covers ∼30 pc in physical size so there are more surrounding massive stars to contribute to the continuum and dilute the WR emission lines, producing a weak excess.

Previous studies use the line ratios of Smith, Shara & Moffat (1996) and Smith, Shara & Moffat (1990) to classify WN and WC subtypes, respectively, along with the Large Magellanic Cloud line luminosities from Crowther & Hadfield (2006) to estimate the number of WN and WC stars within each source. However, M101 is known to be a metal-rich galaxy (Bresolin 2007) and we consistently find our WR sources in solar and supersolar regions (see Section 4.1) so instead we use Galactic templates from observations of WR stars in Rosslowe & Crowther (2015) to estimate the number of WR stars in M101. The templates are adjusted to a Galactic distance of 1 kpc and assume an average extinction for each subtype. The properties of each star used in each template are summarized in Appendix C. We note that for supersolar metallicity regions, such as #1016, the WR emission is expected to be stronger therefore the number of WR stars stated is an upper limit.

Within our 10 WR sources, we have identified 11 WC stars and 4 WN stars. Fig. 3 shows an example of our spectra along with the Galactic template stars whilst additional spectra are presented in Appendix D. We find mid- and late-type WN stars (Smith el al. 1996) in our M101 survey but no early-type WN stars, which is consistent with the online WR Galactic catalogue hosted by Crowther[2] (and references therein), which shows that over 90 per cent of the WR stars classified in the Milky Way to have subtype later than WN5. For our WC stars, we see both WC4-6 and WC7-8 subtypes, indicating a

[2] P.Crowther hosts an up-to-date Galactic WR catalogue at http://pacrowther.staff.shef.ac.uk/WRcat/index.php.

Downloaded from https://academic.oup.com/mnras/article-abstract/473/1/148/4101236
by University of Central Lancashire user
on 02 November 2017

Table 3. Photometric properties of the WR stars spectrographically confirmed in M101. The RA and Dec. positions are taken from the WFC3 *F469N* image.

ID	RA	Dec.	R/R_{25}	m_{F469N}	err	m_{F435W}	err	m_{F555W}	err	m_{F814W}	err	Mask #
56	14:03:25.915	54:20:39.01	0.14	22.59	0.03	23.08	0.02	23.94	0.02	25.23	0.03	1
1030	14:03:16.533	54:20:44.45	0.04	22.92	0.11	23.64	0.46	24.67	0.05	–	–	1
48	14:03:25:286	54:19:17.87	0.18	22.61	0.03	23.56	0.03	24.30	0.03	25.33	0.05	1
1012	14:03:02.861	54:20:11.61	0.11	22.16	0.02	22.62	0.02	23.59	0.03	24.60	0.05	2
1016	14:03:04.711	54:19:24.14	0.13	22.40	0.08	23.20	0.05	24.12	0.05	24.68	0.08	2
49	14:03:23.604	54:19:24.71	0.16	22.43	0.04	23.49	0.01	24.33	0.02	25.65	0.03	4
112	14:03:24.893	54:19:43.16	0.16	22.18	0.09	–	–	22.71	0.04	23.96	0.10	5
114	14:03:29.640	54:22:35.91	0.21	20.70	0.04	20.24	0.06	20.60	0.04	21.68	0.05	5
1024	14:03:13.561	54:19:47.72	0.08	22.67	0.08	23.03	0.02	23.81	0.03	24.74	0.05	6
2053	14:03:32.816	54:20:07.79	0.22	24.83	0.10	–	–	–	–	–	–	6

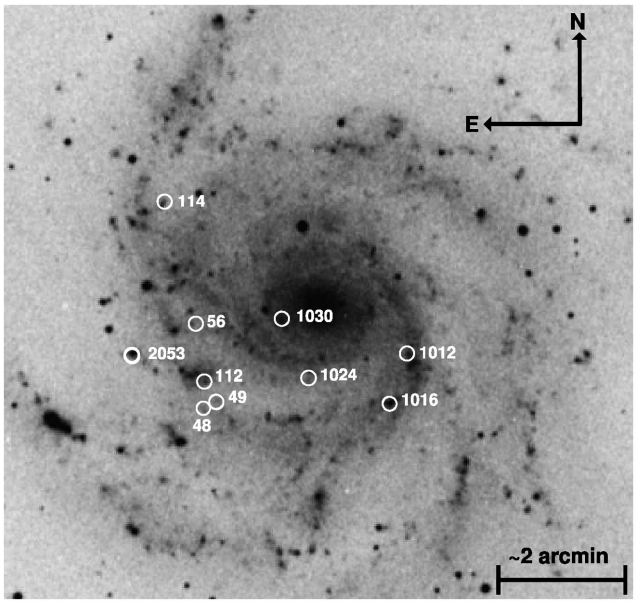

Figure 2. An archival DSS image of M101 showing the location of the spectrographically confirmed WR stars along with their ID's.

trend towards later types but not as clear as for the Galactic sample. Again, small number statistics prevent any firm conclusion.

Interestingly, we see our WN stars located in regions of sub-solar metallicity between log(O/H)+12 = 8.49–8.61, whereas our WC stars favour slightly more metal-rich regions of log(O/H)+12 = 8.69–8.85. This is consistent with stellar evolutionary theory, which predicts that the WC/WN ratio should increase in metal-rich regions due to stronger stellar winds and enhanced stripping of the outer layers (Meynet & Maeder 2005; Eldridge & Vink 2006). Since our WR stars are all within the inner galaxy, we are cautious not to make any direct comparisons but the presence of WN7-8 stars in the most central regions is consistent with the presence of WN9 stars in the inner regions of our own Galaxy. Obtaining spectra of additional WR candidates will allow us to test this theory further. We note that three of our WR sources, including the composite WN+WC source, do not exhibit nebular lines in their spectra so we cannot determine their local metallicity.

4.3 Synthetic magnitudes

As described in Section 3, we used synthetic magnitudes to determine the slit losses for each MOS mask. When comparing the magnitudes derived from the ground-based spectra, we find that the synthetic He II magnitudes are at least 1 mag greater than the WFC3/*F469N* magnitudes in all but one source. This suggests that most of our spectra have multiple stars in the slit, which is

Table 4. Observed fluxes (F_λ) and corrected luminosities (L_λ) for WR stars in M101 confirmed with Gemini/GMOS observations. Errors on the line fluxes are shown in parenthesis. Sources are corrected for slit loss and dereddened using the extinction determined from the nebular emission in the spectrum. Where no nebular emission is present a value of $E(B-V) = 0.44$ is taken from Lee et al. (2009) and luminosities are based on a distance of 6.4 Mpc from Shappee & Stanek (2011). WN and WC numbers are derived from Galactic WR templates from Rosslowe & Crowther (2015).

		F_λ ($\times 10^{-16}$ erg s^{-1} cm^{-2})							L_λ ($\times 10^{36}$ erg s^{-1})			
ID	R/R_{25}	*F*(N III) λ4612-30	*F*(C III) λ4650	*F*(He II) λ4686	*F*(He II) λ5411	*F*(C III) λ5696	*F*(C IV) λ5808	$E(B-V)$	*L*(He II) λ4686	*L*(C IV) λ5808	*N*(WN)	*N*(WC)
56	0.14	–	1.27(0.14)	1.35(0.14)	0.54(0.12)	–	1.64(0.14)	0.44	3.19	2.56	1 × WN4-6	2 × WC4-6
1030	0.04	–	1.10(0.17)	1.22(0.23)	–	0.92(0.26)	0.76(0.19)	0.44	2.84	1.23	–	2 × WC7-8
48	0.18	–	–	3.17(0.40)	–	–	–	0.14	2.62	–	1 × WN4-6	–
1012	0.11	–	3.83(0.54)	2.58(0.47)	–	–	3.69(1.18)	0.09	1.68	2.24	–	1 × WC4-6
1016	0.13	–	11.6(1.68)	6.13(1.56)	–	6.27(0.68)	2.38(0.48)	0.59	13.8	12.0	–	1 × WC7-8
49	0.16	–	5.07(0.27)	–	–	–	1.88(0.12)	0.12	–	1.33	–	3 × WC4-6
112	0.16	–	–	1.93(0.40)	–	–	–	0.53	5.25	–	1 × WN7-8	–
114	0.21	–	1.45(0.33)	–	–	–	1.23(0.32)	0.44	–	2.49	–	1 × WC4-6
1024	0.08	–	1.86(0.30)	–	–	1.00(0.15)	0.24(0.11)	0.46	–	0.28	–	1 × WC7-8
2053	0.22	6.3(0.11)	–	6.59(0.16)	–	–	–	0.98	90.7	–	1 × WN7-8	–

Downloaded from https://academic.oup.com/mnras/article-abstract/473/1/148/4101236
by University of Central Lancashire user
on 02 November 2017

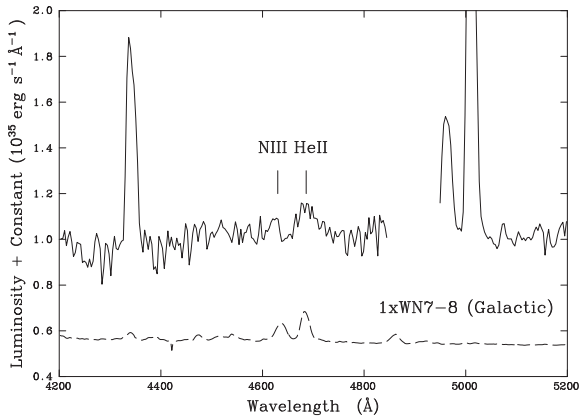

(a) Source #112

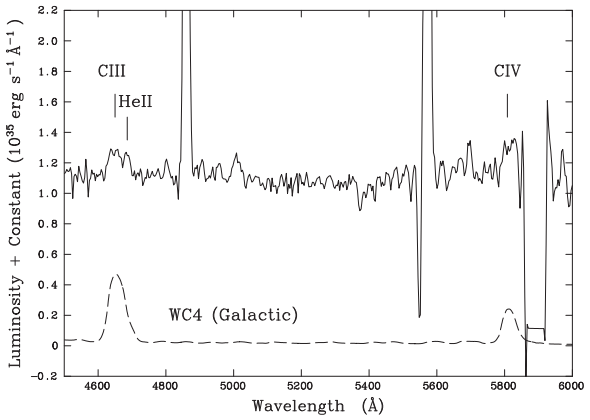

(b) Source #1012

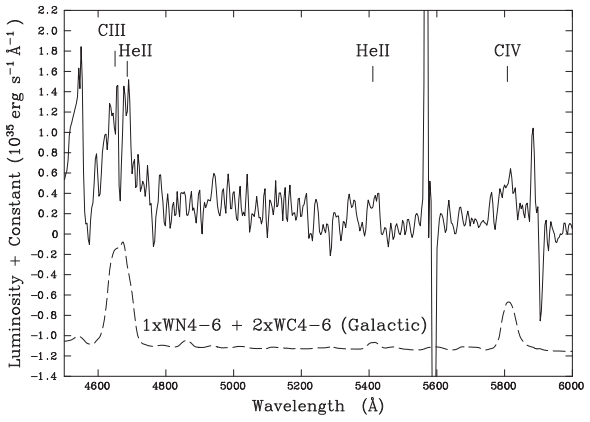

(c) Source #56

Figure 3. Normalized, extinction and distance corrected spectra of WR sources in M101 along with Galactic WR template spectra from Rosslowe & Crowther (2015). The units shown are Luminosity per unit wavelength. Source (a) shows a single WN7-8 star, (b) a single WC4 star and (c) a composite of one WN4-6 and two WC4-6 stars. The template spectra are offset from the observed spectra for clarity. We note the feature just short of 4600 Å in Source #56 is due to the chip gap extrapolation with the Gemini packages and is not real.

unsurprising given the 0.8 arcsec versus 0.1 arcsec resolution difference. This is further highlighted in the 2×2 arcmin^2 images of each source presented in Appendix A where additional sources can be seen within 1 arcsec (our GMOS slit size) of each WR candidate with the exception of Source #56. Unsurprisingly, Source #56 is the only source where the WR component dominates the spectra, indicating an He II excess of –1.16 mag. The crowding owing to the 1 arcsec slit width results in a synthetic He II excess of a m(He II) – m(Continuum) excess $\leq$–0.15 mag for all but one source (#49). This excess is within typical errors of ground-based photometry and as such these WR stars would not have been identified as WR candidates from ground-based imaging such as that presented in Bibby & Crowther (2012).

4.4 Non-detections

In total, 208 WR candidates were included in the seven MOS mask designs. There was an error in the coordinate transformation from the *HST* imaging to the GMOS pre-imaging so one MOS mask (#7) yielded no WR spectra. In addition, we used one MOS mask (#4) to try to acquire spectra of the faintest WR stars with $m_{F435W} \leq 24$ mag; however, none of these 17 candidates in this mask were extracted successfully. This reduced the total number of WR candidates to 159 sources.

Out of these 19 per cent of spectra revealed nebular lines, 11 per cent absorption lines, 7 per cent WR emission lines and 3 per cent had the He II λ4686 emission line located in a chip gap. We hoped to avoid diagnostic lines falling into chip gaps by using two central wavelengths; however, the combined spectra often was not clean enough to identify a WR emission line confidently. Unfortunately, the remaining spectra showed only noise or could not be extracted. On further inspection, the majority of our WR candidates had $m_{F435W} \leq 24$ mag in the continuum so it is not surprising that they could not be extracted as was found with MOS mask #4.

No WR stars fainter than $m_{F435W} = 23.64$ mag were detected by Gemini/GMOS and we note for future observations that this limits us to the brighter stars in M101. Moreover, the photometry presented in Table 3 indicates that the WR stars had m_{F435W}–m_{F469N} excesses $\geq$0.36 mag suggesting that our GMOS survey is favouring the strongest emission-line stars. None the less the WR stars, we have detected are strongly supportive of our identification of candidates as WR stars. We expect that a number of the objects, we were unable to detect as WR strs in these observations will ultimately be shown to be WR stars, as their luminosity function suggests. To confirm this, however, more sensitive observations will be required.

5 WR STARS IN H II REGIONS

H II regions are formed and powered by the ionizing radiation produced by massive O stars. The number of O stars and amount of ionizing radiation influences the size of the H II region. Classical H II regions contain only a handful of O stars and are typically of the order of 10 pc in diameter. Giant H II regions are of the order of $\sim$100 pc in size, hosting $\sim$100 O7 V stars. However, giant H II regions often host separate star-forming regions of different sizes and ages so there is not a direct size–luminosity correlation. Since only O stars are capable of producing such regions, one would expect O stars, WR stars and resulting ccSNe to be associated with such H II regions. However, in the Milky Way only 27 per cent of WR stars are seen to be associated with such regions (Crowther 2015), which is most likely due to the fact that they are ejected or that the star-forming region is unbound so dissolves quickly (Crowther 2013). It is also possible that the H II region fades quicker than the average lifetime of the WR stars or that the cluster itself may still be embedded due to its young age (Gvaramadze et al. 2012); rarely these stars might also form in isolation.

Downloaded from https://academic.oup.com/mnras/article-abstract/473/1/148/4101236
by University of Central Lancashire user
on 02 November 2017

Table 5. Hα +[N II] flux measurements of the H II regions confirmed to host WR stars. We note that the radius of the H II region is largely influenced by the spatial resolution of the images and is quoted for information only. The Hα flux is corrected for distance, extinction and [N II] contribution and the Hα luminosity is determined using the calibration of Knapen et al. (2004) and the N(07 v) stars using 10^{49} photons s^{-1} (Vacca 1994).

WR ID	Hodge ID	RA[a] (h:m:s)	Dec.[a] (°:′:″)	Radius (arcsec)	F(Hα +[N II]) (erg s^{-1} cm^{-2})	$E(B-V)$	[N II]/ Hα	L(Hα) (erg s^{-1})	log Q_0 (s^{-1})	N(O7 v)	N(WR)/ N(O7 v)	Spectra	KPNO	*HST*
56												No	No	No
1030	733	14:03:10.786	54:20:18.34	3.32	4.29×10^{-14}	0.44	0.54	3.71×10^{38}	50.44	28	0.07	No	Edge	Edge
48												Yes	No	Yes
1012	470	14:03:07.184	54:22:21.02	4.22	7.69×10^{-14}	0.09	0.35	3.79×10^{38}	50.17	15	0.14	Yes	Yes	Yes
1016	505, 507	14:03:01.800	54:22:03.87	6.27	3.08×10^{-13}	0.59	0.63	3.39×10^{39}	51.40	250	0.004	Yes	Yes	Yes
49	872	14:03:02.108	54:19:16.07	2.34	5.11×10^{-15}	0.12	0.67	5.37×10^{37}	49.60	4	0.75	Yes	Yes	Edge
112	901	14:03:04.219	54:19:05.39	3.86	7.49×10^{-14}	0.53	0.30	1.30×10^{39}	50.98	96	0.01	Yes	Yes	Yes
114	998	14:03:23.969	54:18:24.57	3.37	5.56×10^{-14}	0.44	0.54	1.93×10^{39}	51.16	145	0.007	No	Yes	Edge
1024	671	14:03:04.531	54:20:45.32	2.90	1.63×10^{-14}	0.46	0.22	2.39×10^{38}	50.25	18	0.06	Yes	Yes	Yes
2053	1044	14:03:07.460	54:17:55.79	6.87	3.88×10^{-13}	0.98	0.14	3.28×10^{40}	52.39	2454	0.0004	Yes	Yes	Edge

[a]Co-ordinates of the H II region are taken from the KPNO Hα image in Knapen et al. (2004).

In addition to investigating the association with H II regions, we can also estimate the O star population itself. We have used flux calibrated KPNO/JAG Hα images from Knapen et al. (2004), corrected for extinction and [N II] contamination, to determine the Hα luminosity for each region. Using the relation of Kennicutt (1998), we can determine the number of ionizing photons from the strength of the Hα emission, which, in turn, allows us to estimate the number of O stars present, assuming 10^{49} photons s^{-1} for an O7V star (Vacca 1994). For six of our WR sources, we can compare the WR/O7V ratio as a function of metallicity to predictions from evolutionary models (such as Eldridge & Vink 2006) but with so few points it is not possible to make any helpful comparison. Also, we do not account for the contribution of WR stars to the ionizing photons (Vacca & Conti 1992). For example, in Source #49 the 3 WC stars present would be expected to contribute significantly towards the ionizing flux so the WR/O = 0.75 ratio is a lower limit since the number of O stars is not required to be as high to account for the measured flux. Our full survey of M101 will allow us to investigate this in more detail.

We have identified whether a WR star is directly in, on the edge of an H II region or is truly isolated and have identified the region from Hodge et al. (1990) and use their nomenclature in this work. Aperture photometry was performed in GAIA and each aperture size was determined based on a 95 per cent luminosity cut with background subtraction performed by using an additional aperture of the same radius on an 'empty' region local to the H II region. The corresponding aperture radii, luminosity measurements and resulting O star population for each source are presented in Table 5. The error on the final number of O stars is ∼10 per cent, which results from the choice of aperture size, although this does not account for the error associated with the ionizing flux from WR stars; the errors on the flux measurements themselves are of the order of 1 per cent.

A total of 7 out of our 10 sources exhibit Hα emission in their spectra, from which we conclude that 70 per cent of WR stars in M101 are found in H II regions (based on small number statistics of course). On inspection of archival KPNO imaging (Knapen et al. 2004), we also conclude that 70 per cent of WR stars are in H II regions; however, there are discrepancies between the imaging and spectroscopic data.

Source #112 is directly located in an H II region in both archival KPNO and *HST* narrow-band Hα imaging and, as one would expect, shows nebular emission lines in its spectrum. Conversely, the spectrum of Source #114 does not show nebular emission but does

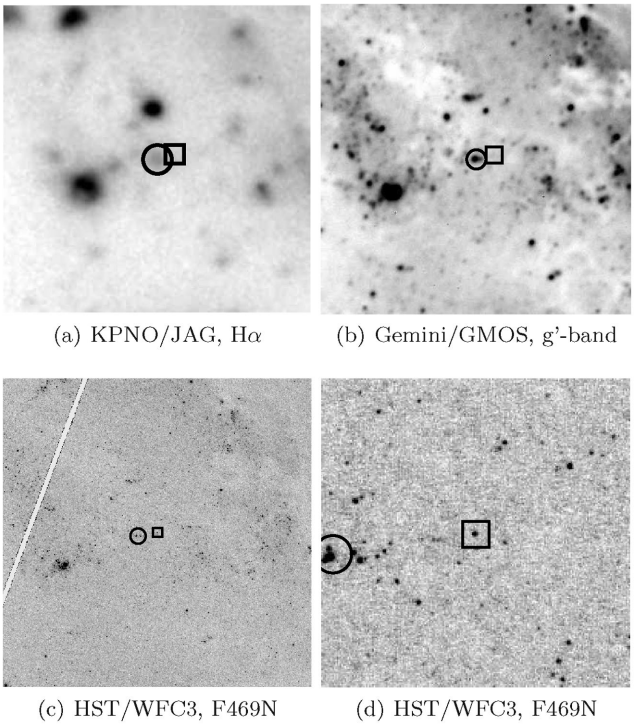

(a) KPNO/JAG, Hα (b) Gemini/GMOS, g'-band

(c) HST/WFC3, F469N (d) HST/WFC3, F469N

Figure 4. Postage stamp images of ∼1 arcmin showing the location of WR Source #56 (square) and associated H II region #937 (circle) as observed with different telescopes (a)–(c). Image (d) is a close up on (c) clearly identifying the WR star. The orientation of the images is North up and East left.

show stellar absorption features typical of a main-sequence A star along with WR emission lines. Ground-based KPNO imaging suggests that the source is in an H II region, however, the superior spatial resolution of *HST*/ACS imaging reveals that the source is actually ∼2 arcsec north-west of the H II region. We note that the resolution of the KPNO imaging is ∼2.5 arcsec.

The lack of nebular emission in Source #56 is consistent with no Hα detection in the KPNO imaging (Fig. 4). Since the spectrum of Source #56 reveals the presence of both WN and WC stars, it is likely that the H II region is beyond the detection limits of the KPNO imaging. In addition, archival *HST F658N* imaging does not reveal the presence of an H II region, suggesting that the gas from

Downloaded from https://academic.oup.com/mnras/article-abstract/473/1/148/4101236
by University of Central Lancashire user
on 02 November 2017

the star cluster has been expelled. The projected distance of Source #56 from the closest cluster is ∼150 pc, which is consistent with the distance a runaway WR star can travel in its lifetime (Eldridge, Langer & Tout 2011). The presence of multiple WR stars in the GMOS spectrum makes this scenario unlikely.

The spectrum of Source #1030 has a chip gap at the location of the H$\alpha\lambda$6563 emission, but the star but is located on the edge of an H II region in the KPNO image, which the *HST* imaging reveals to be a stream connecting two H II regions. The most likely explanation is that the spatially extended Hα emission is too weak to be detected in the GMOS spectra. Interestingly, Source #48 does show Hα emission in its spectrum; however, the KPNO imaging does not reveal any H II region. This would suggest that there is a faint, underlying H II region beyond the detection limits of the KPNO data, which is confirmed to be the case from archival *HST* *F*658*N* imaging.

In addition to #112, a further three of our WR Sources, #1012, 1016 and 1024 present a nebular spectrum and are located in H II regions seen in both KPNO and *HST* imaging. Although Sources #49 and #2053 exhibit Hα emission in the GMOS spectroscopy and KPNO imaging the resolution of *HST* reveals that they are in fact on the edge of the H II region, suggesting that the spectroscopic detection is of the H II region itself. The location of each WR source relative to the Hα emission is presented in Appendix A.

In summary, from KPNO Hα imaging we conclude that 70 per cent of WR stars in our sample are in H II regions, 10 per cent are associated with H II regions and 20 per cent are not associated with H II regions. However, from the improved spatial resolution of *HST* our conclusions are 50 per cent in, 40 per cent associated with and 10 per cent not in H II regions. The high fraction of WR stars being associated with H II regions is not consistent with the low fraction (27 per cent) of WR stars associated with star-forming regions presented by Crowther (2015). Whilst we do not claim these results to be statistically robust due to small number statistics, the difference between the conclusions based on the two sets of imaging, particularly between those directly in or on the edge of an H II region, demonstrates how the spatial resolution and sensitivity of imaging can lead to different interpretations of stellar environment. Moreover, the spectroscopic results presented here are limited to the brighter WR stars, which are more likely to be found in bright H II regions. We expect a full spectroscopic survey, including the fainter WR candidates to reduce the fraction of WR stars seen in H II regions.

6 SUMMARY

We spectrographically confirmed the detection of 15 WR stars within 10 He II emission sources in M101. From comparison with Galactic templates, we conclude that these regions host 4 WN and 11 WC stars, indicating that our detections are biased towards WC stars. This is not surprising given the higher He II excess for WC stars compared to WN stars. Moreover, all of our regions are metal-rich so we expect a WC/WN ratio $\geq$1 based on the evolutionary models from Eldridge & Vink (2006), which is consistent with our findings though our sample is limited by small number statistics.

We see no distinctive division between the locations of WC and WN stars, though again, our sample is small. The successful detection of both WC and WN stars demonstrates that our imaging technique is sensitive to both, including the coolest WC and WN stars, WC7-8 and WN7-8, respectively.

The main challenge to spectroscopically confirming WR stars in M101 is the required line to continuum contrast, since the He II excess, or line-to-continuum ratio, is our primary diagnostic for identifying WR candidates. This can be hindered by intrinsically weak WR emission (e.g. in low-metallicity environments) hence high S/N observations are required in future to confirm these candidates as bona fide WR stars. A companion star or surrounding massive stars within the same slit will also increase the continuum and dilute the WR emission line making the confirmation of a WR more difficult; high-resolution observations are required to overcome this as well as careful mapping of sources from *HST* imaging to ground-based spectra.

ACKNOWLEDGEMENTS

This research is based on spectroscopic observations obtained at the Gemini Observatory, which is operated by the Association of Universities for Research in Astronomy, Inc., under a cooperative agreement with the NSF on behalf of the Gemini partnership: the National Science Foundation (United States), the National Research Council (Canada), CONICYT (Chile), the Australian Research Council (Australia), Ministério da Ciência, Tecnologia e Inovação (Brazil) and Ministerio de Ciencia, Tecnología e Innovación Productiva (Argentina). Photometric results presented here are based on NASA/ESA *HST* observations obtained at the Space Telescope Science Institute, which is operated by the Association of Universities for Research in Astronomy Inc. under NASA contract NAS5-26555. JLB, MMS and MW acknowledge the interest and generous support of Hilary and Ethel Lipsitz. AFJM is grateful to NSERC (Canada) and FQRNT (Quebec) for financial assistance.

REFERENCES

Bibby J. L., Crowther P. A., 2010, MNRAS, 405, 2737
Bibby J. L., Crowther P. A., 2012, MNRAS, 420, 3483
Bresolin F., 2007, ApJ, 656, 186
Cao Y. et al., 2013, AJ, 775, L7
Cedrés B., Cepa J., 2002, A&A, 391, 809
Cedrés B., Urbaneja M. A., Cepa J., 2004, A&A, 422, 514
Chomiuk L., Povich M. S., 2011, AJ, 142, 197
Conti P. S., Vacca W. D., 1990, AJ, 100, 431
Crockett R. M. et al., 2007, MNRAS, 381, 835
Crowther P. A., 2013, MNRAS, 428, 1927
Crowther P. A., 2015, in Hamann W. R., Sander A., Todt H., eds, Wolf-Rayet Stars: Proc. Int. Workshop. Universitatsverlag Potsdam
Crowther P. A., Hadfield L. J., 2006, A&A, 449, 711
Crowther P. A., Barnard R., Carpano S. et al., 2010, MNRAS, 403, L41
Drissen L., Roy J.-R., Moffat A. F. J., Shara M. M., 1999, AJ, 117, 1249
Eldridge J. J., Vink J. S., 2006, A&A, 452, 295
Eldridge J. J., Langer N., Tout C. A., 2011, MNRAS, 414, 3501
Eldridge J. J., Fraser M., Smartt S. J., Maund J. R., Crockett M. R., 2013, MNRAS, 436, 774
Gies D. R. et al., 2003, ApJ, 583, 424
Groh J. H., Georgy C., Ekström S., 2013, A&A, 558, L1
Gvaramadze V. V., Weidner C., Kroupa P., Pflamm-AAltenburg J., 2012, MNRAS, 424, 3037
Hadfield L. J., Crowther P. A., Schild H., Schmutz W., 2005, A&A, 439, 265
Hodge P. W., Gurwell M., Goldader J. D., Kennicutt R. C., Jr, 1990, ApJS, 73, 661
Howarth I. D., Murray J., Mills D., Berry D. S., 2004, Starlink User Note 50, Starlink Project
Jarrett T. H. et al., 2013, AJ, 145, 6
Karamehmetoglu E. et al., 2017, A&A, 602, 93
Kenney J. D. P., Lord S. D., 1991, ApJ, 381, 118
Kennicutt R. C., Jr, 1998, ARA&A, 36, 189
Kennicutt R. C., Jr, Lee J. C., Funes S. J., José G., Sakai S., Akiyama S., 2008, ApJS, 178, 247

Downloaded from https://academic.oup.com/mnras/article-abstract/473/1/148/4101236
by University of Central Lancashire user
on 02 November 2017

Knapen J. H., Stedman S., Bramich D. M., Folkes S. F., Bradley T. R., 2004, A&A, 426, 1135
Lee J. C. et al., 2009, ApJ, 706, 599
Leloudas G. et al., 2011, A&A, 530, 95
Liu J., Bregman J. N., Bai Y., Justham S., Crowther P. A., 2013, Nature, 503, 500
Massey P., Johnson O., 1998, ApJ, 505, 793
Maund J. R., Mattila S., Ramirez-Ruis E., Eldridge J. J., 2014, MNRAS, 438, 1577
Meynet G., Maeder A., 2005, A&A, 429, 581
Moffat A. J., Shara M. M., 1983, ApJ, 273, 544
Neugent K. F., Massey P., 2011, ApJ, 733, 123
Oke J. B., 1990, AJ, 99, 1621
Orosz J. A. et al., 2007, Nature, 449, 872
Osterbrock D. E., Ferland G. J., 2006, 'Astrophysics of Gaseous Nebulae and Active Galactic Nuclei', 2nd. ed. University Science Books, Sausalito, CA
Pettini M., Pagel B. E. J., 2004, MNRAS, 348, L59
Pilyugin L. S., Thuan T. X., 2005, ApJ, 631, 231
Prestwich A. H. et al., 2007, ApJ, 669, 21
Rosa M. R., Benvenuti P., 1994, A&A, 291, 1
Rosslowe C. K., Crowther P. A., 2015, MNRAS, 447, 2322
Shappee B. J., Stanek K. Z., 2011, ApJ, 733, 124
Shara M. M., Bibby J. L., Zurek D., Crowther P. A., Moffat A. F. J., Drissen L., 2013, AJ, 146, 162
Shortridge K. et al., 2004, Starlink User Note 86, Starlink Project
Silverman J. M., Filippenko A. V., 2008, ApJ, 678, 17
Smartt S. J., 2009, ARA&A, 47, 63
Smith L. F., Shara M. M., Moffat A. F. J., 1990, ApJ, 358, 229
Smith L. F., Shara M. M., Moffat A. F. J., 1996, MNRAS, 281, 163
Smith N., Li W., Filippenko A., Chornock R., 2011, MNRAS, 412, 1522
Vacca W. D., 1994, ApJ, 421, 140
Vacca W. D., Conti P. S., 1992, ApJ, 401, 543

APPENDIX A: LOCATION OF WR SOURCES IN RELATION TO H II REGIONS

Postage stamp images of ∼1 arcmin showing the location of the H II region closest to the WR source. Circles indicate the location of the H II region in (a)–(c) and of the WR star in (d). Where the WR star is located outside the H II region a square has been used to identify it's location.

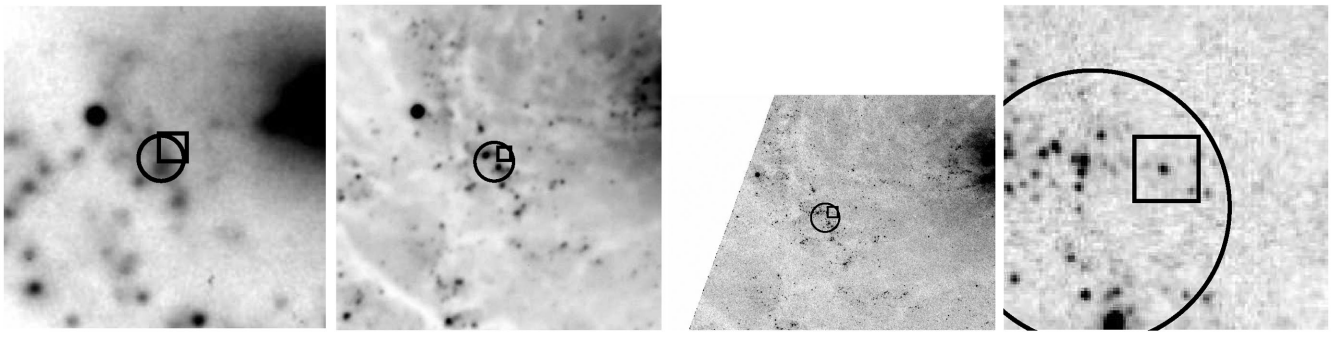

Figure A1. Source #1030.

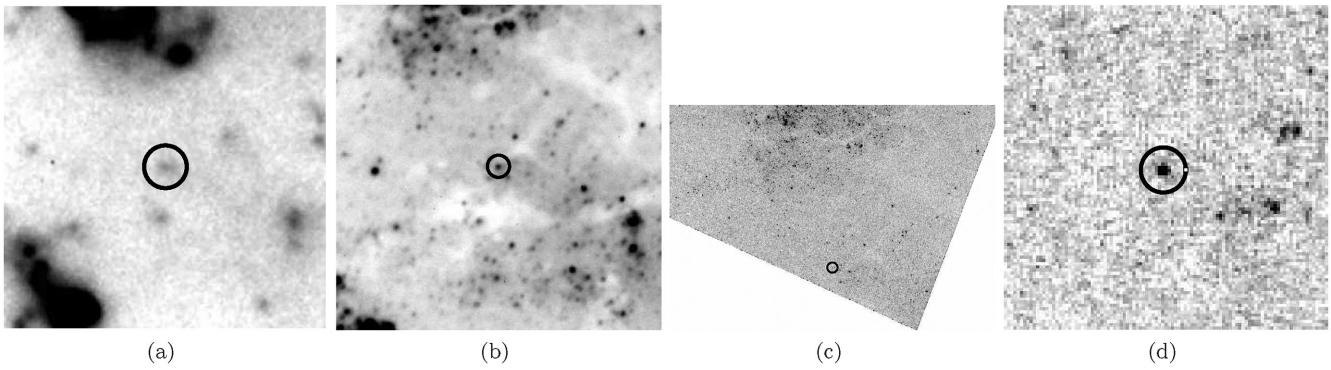

Figure A2. Source #48.

Downloaded from https://academic.oup.com/mnras/article-abstract/473/1/148/4101236
by University of Central Lancashire user
on 02 November 2017

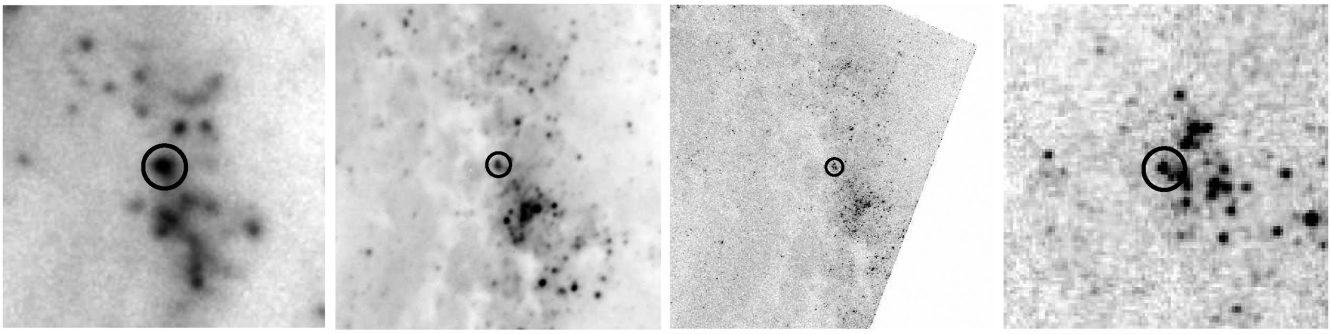

Figure A3. Source #1012.

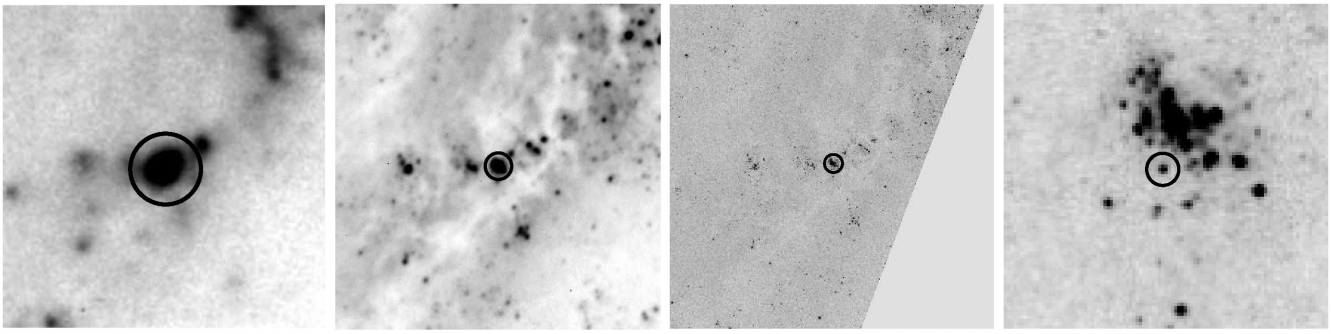

Figure A4. Source #1016.

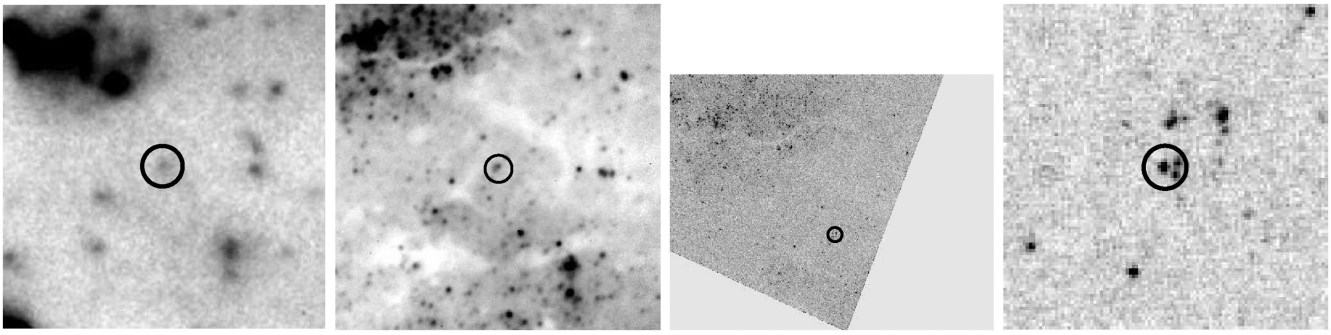

Figure A5. Source #49.

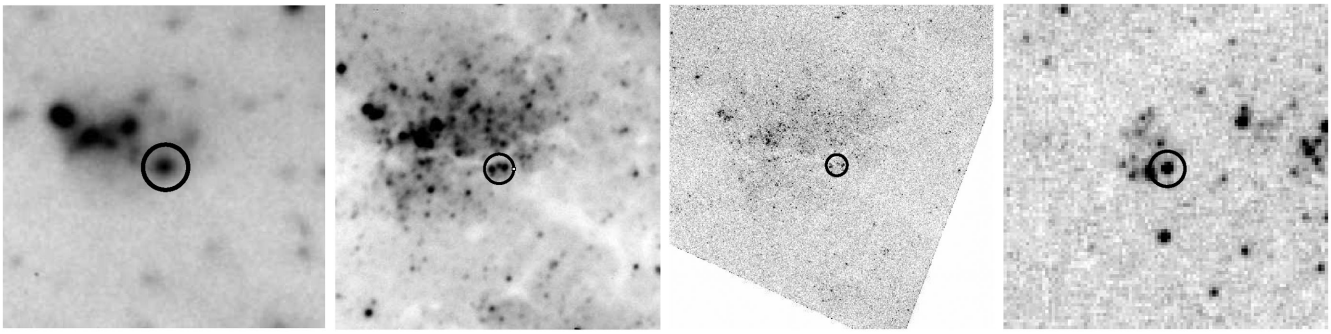

Figure A6. Source #112.

Downloaded from https://academic.oup.com/mnras/article-abstract/473/1/148/4101236
by University of Central Lancashire user
on 02 November 2017

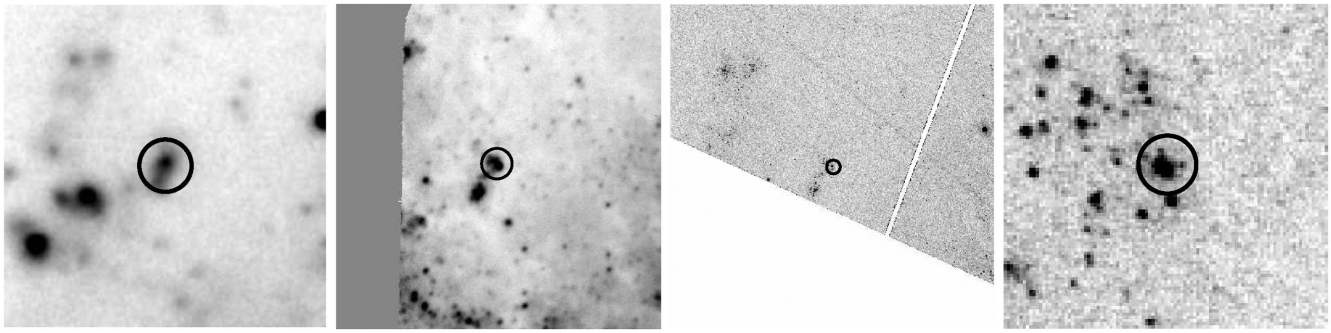

Figure A7. Source #114.

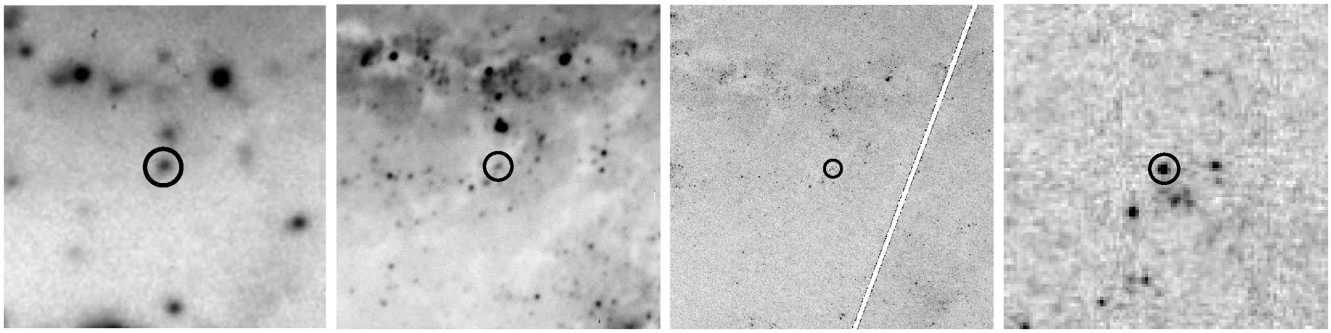

Figure A8. Source #1024.

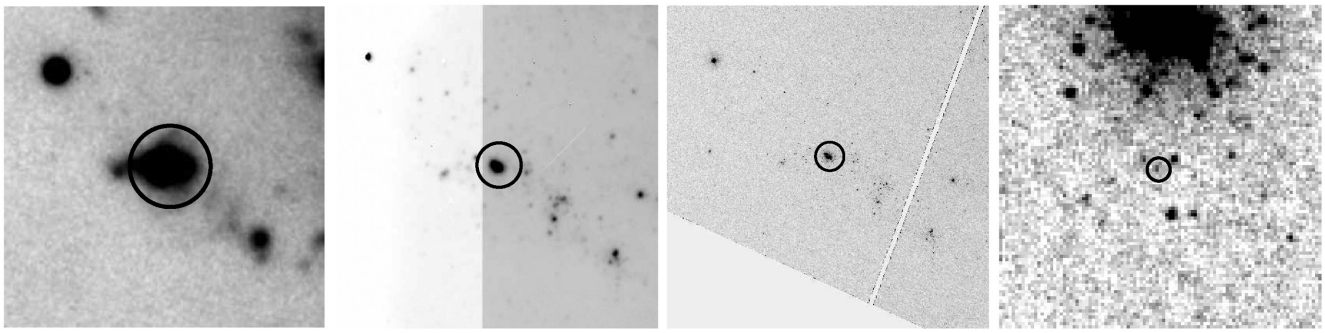

Figure A9. Source #2053.

Downloaded from https://academic.oup.com/mnras/article-abstract/473/1/148/4101236
by University of Central Lancashire user
on 02 November 2017

APPENDIX B: FINDING CHARTS FOR WR STARS

This appendix contains 2 × 2 arcmin^2 stamps of each WR star in the (a) F469N, (b) F435W, (c) F555W, (d) F814W and (e) continuum subtracted F469N filters.

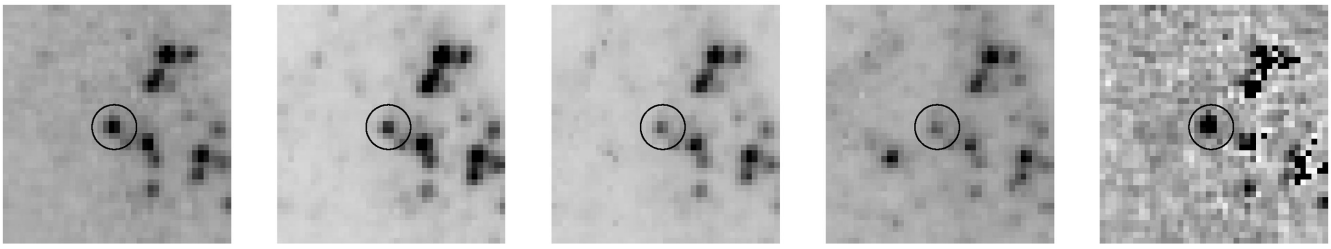

Figure B1. Source #1012 in *F*469*N*, *F*435*W*, *F*555*W*, *F*814*W* and continuum subtracted *F*469*N* filters, respectively.

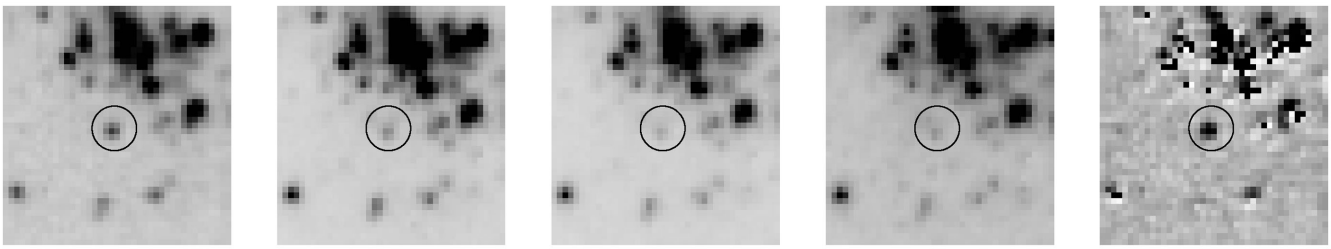

Figure B2. Source #1016 in *F*469*N*, *F*435*W*, *F*555*W*, *F*814*W* and continuum subtracted F469N filters, respectively.

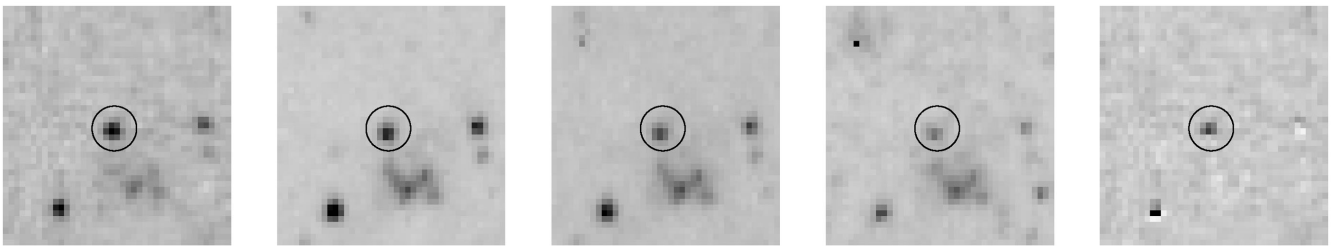

Figure B3. Source #1024 in *F*469*N*, *F*435*W*, *F*555*W*, *F*814*W* and continuum subtracted *F*469*N* filters, respectively.

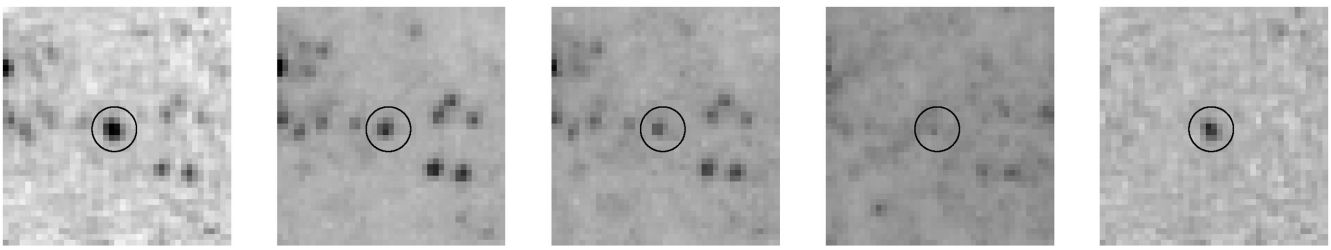

Figure B4. Source #1030 in *F*469*N*, *F*435*W*, *F*555*W*, *F*814*W* and continuum subtracted *F*469*N* filters, respectively.

Downloaded from https://academic.oup.com/mnras/article-abstract/473/1/148/4101236
by University of Central Lancashire user
on 02 November 2017

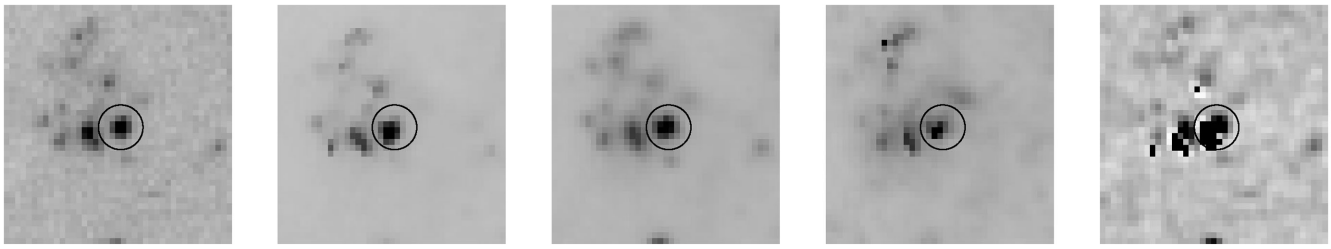

Figure B5. Source #112 in *F*469*N*, *F*435*W*, *F*555*W*, *F*814*W* and continuum subtracted *F*469*N* filters, respectively.

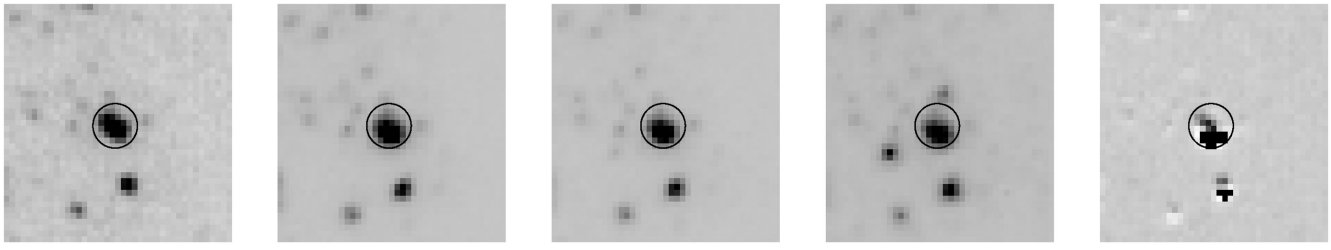

Figure B6. Source #114 in *F*469*N*, *F*435*W*, *F*555*W*, *F*814*W* and continuum subtracted *F*469*N* filters, respectively.

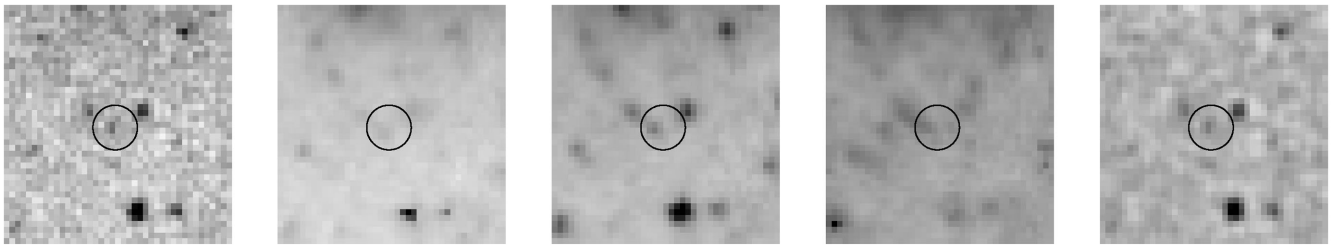

Figure B7. Source #2053 in *F*469*N*, *F*435*W*, *F*555*W*, *F*814*W* and continuum subtracted *F*469*N* filters, respectively.

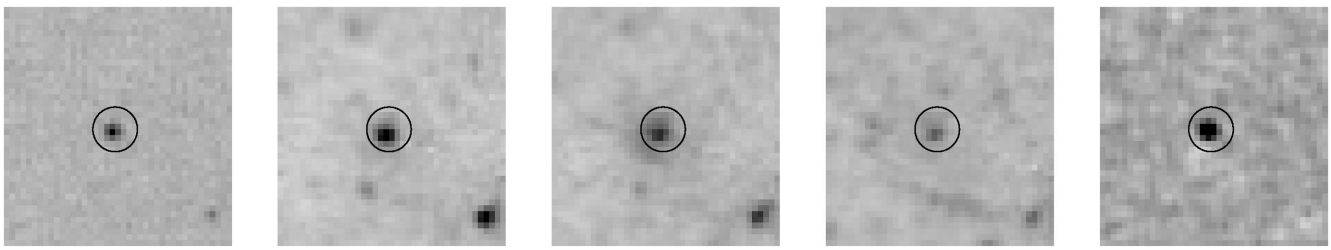

Figure B8. Source #48 in *F*469*N*, *F*435*W*, *F*555*W*, *F*814*W* and continuum subtracted *F*469*N* filters, respectively.

Downloaded from https://academic.oup.com/mnras/article-abstract/473/1/148/4101236
by University of Central Lancashire user
on 02 November 2017

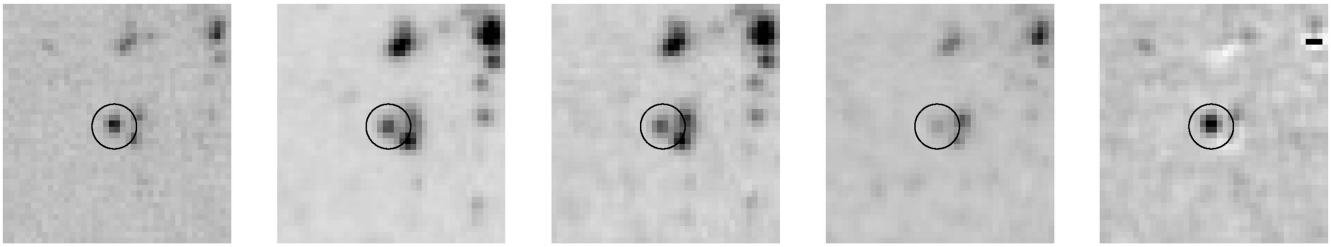

Figure B9. Source #49 in *F*469*N*, *F*435*W*, *F*555*W*, *F*814*W* and continuum subtracted *F*469*N* filters, respectively.

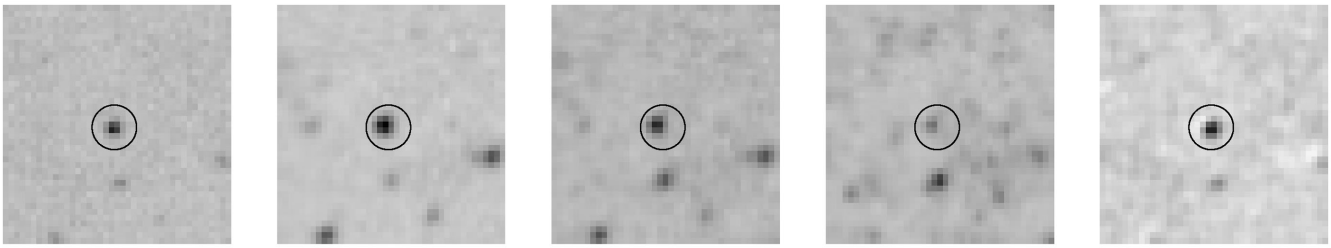

Figure B10. Source #56 in *F*469*N*, *F*435*W*, *F*555*W*, *F*814*W* and continuum subtracted *F*469*N* filters, respectively.

APPENDIX C: DATA FOR GALACTIC FLUX TEMPLATES

Table C1. This appendix contains information regarding the Galactic WR stars used to produce the flux templates used in this analysis, taken from Rosslowe & Crowther (2015) and will be updated following the *GAIA* DR2 release.

ID	Subtype	Distance (kpc)	$E(B-V)$
WN4-6 template			
WR1	WN4b	2.3	1.09
WR6	WN4b	1.8	0.17
WR7	WN4b	5.5	0.69
WR18	WN4b	2.3	0.91
WR134	WN6b	1.9	0.50
WR136	WN6b	1.3	0.59
WN7-8 template			
WR12	WN7	4.2	0.72
WR66	WN8	3.6	1.12
WC4-6			
WR144	WC4	1.4	2.65
WR111	WC5	1.9	0.34
WR114	WC5	2.05	1.45
WR23	WC6	2.3	0.42
WR154	WC6	3.5	0.78
WC7-8 template			
WR14	WC7	2.2	0.57
WR68	WC7	3.6	1.55
WR135	WC8	1.9	0.28
WR53	WC8d	4.2	0.58

Downloaded from https://academic.oup.com/mnras/article-abstract/473/1/148/4101236
by University of Central Lancashire user
on 02 November 2017

APPENDIX D: SPECTRA FOR EACH WR SOURCE

This appendix contains the flux calibrated Gemini/GMOS spectra of each WR source. Also shown is the best-fitting Galactic WR template spectra from Rosslowe & Crowther (2015).

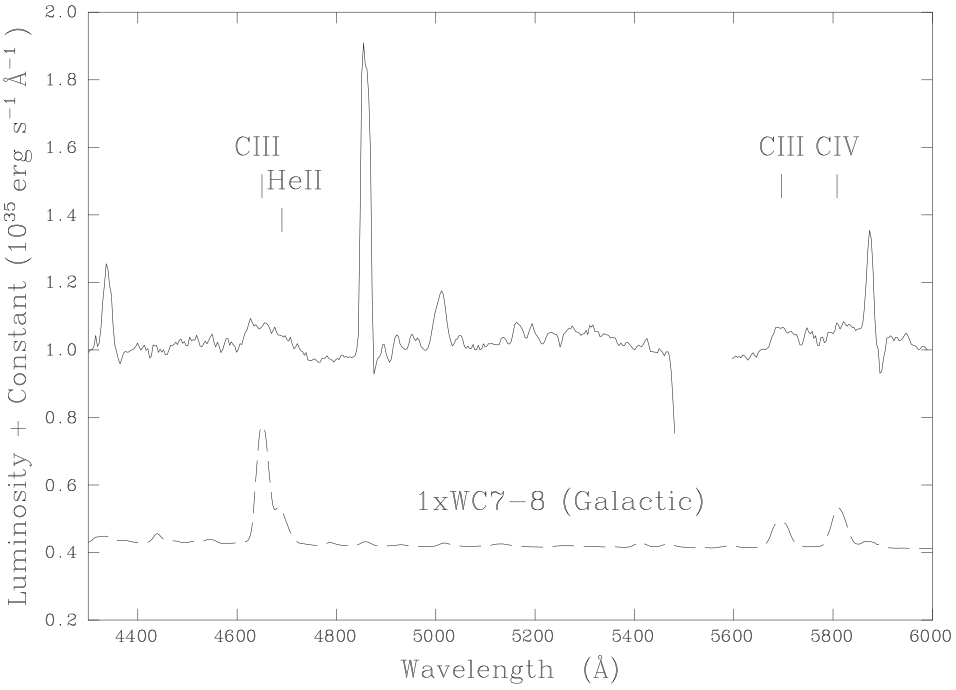

Figure D1. Spectrum of Source #1016.

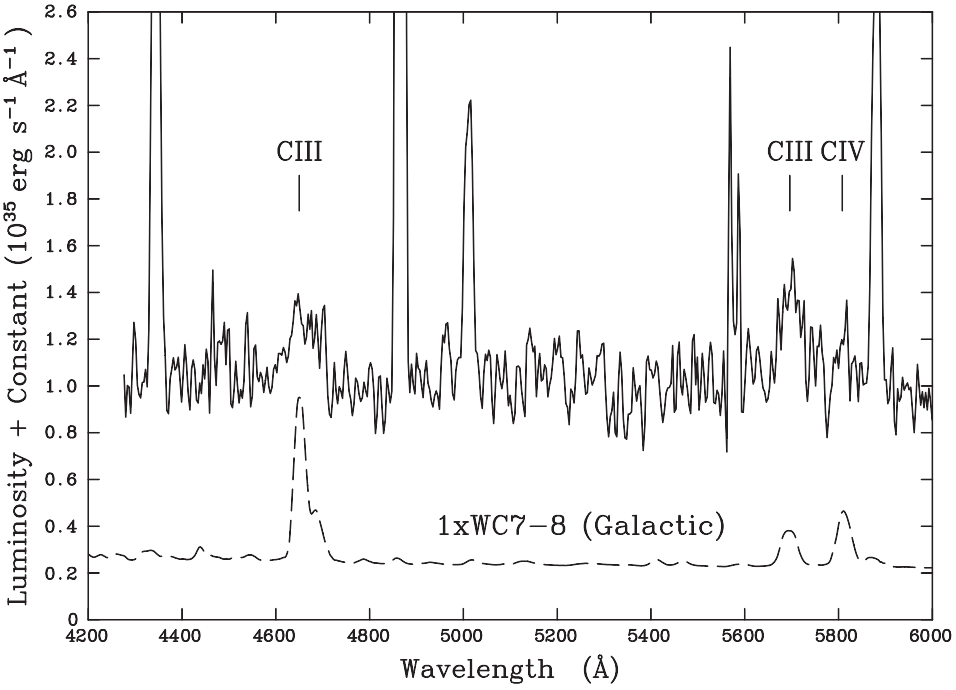

Figure D2. Spectrum of Source #1024.

Downloaded from https://academic.oup.com/mnras/article-abstract/473/1/148/4101236
by University of Central Lancashire user
on 02 November 2017

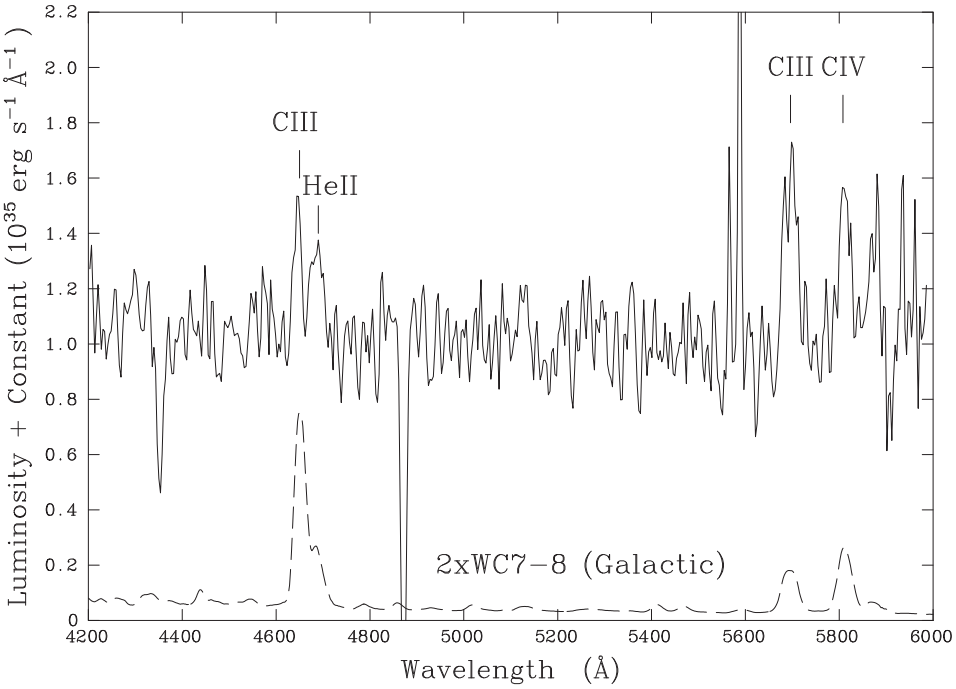

Figure D3. Spectrum of Source #1030.

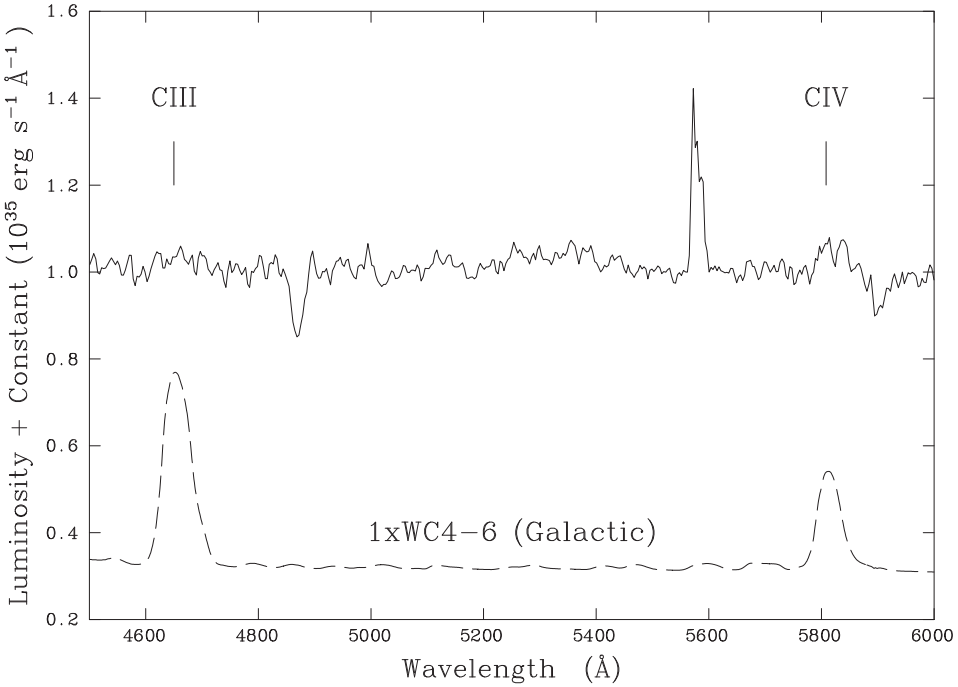

Figure D4. Spectrum of Source #114.

Downloaded from https://academic.oup.com/mnras/article-abstract/473/1/148/4101236
by University of Central Lancashire user
on 02 November 2017

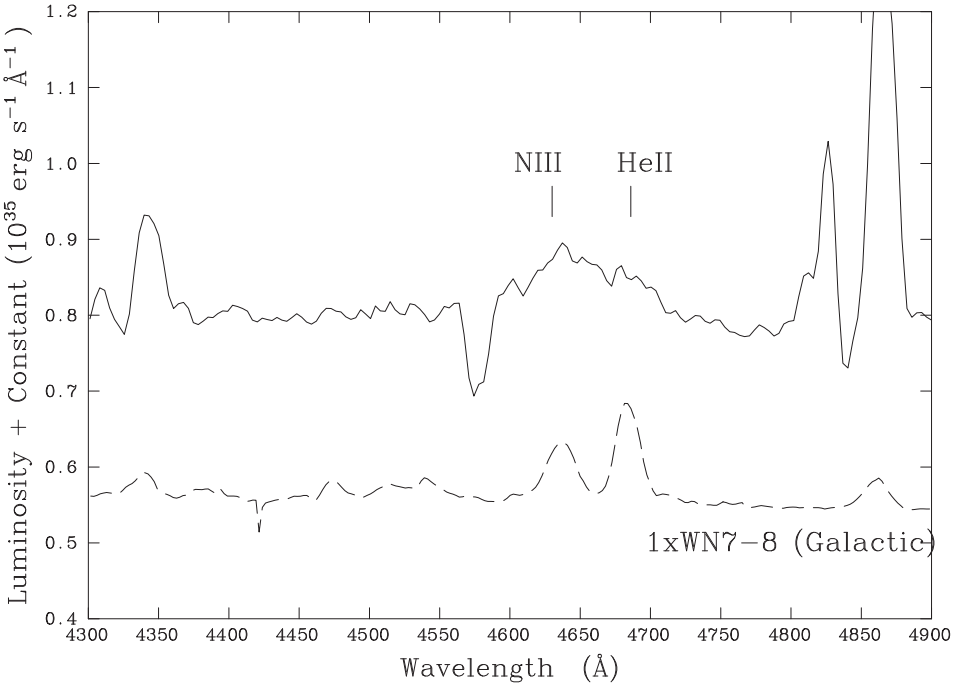

Figure D5. Spectrum of Source #2053.

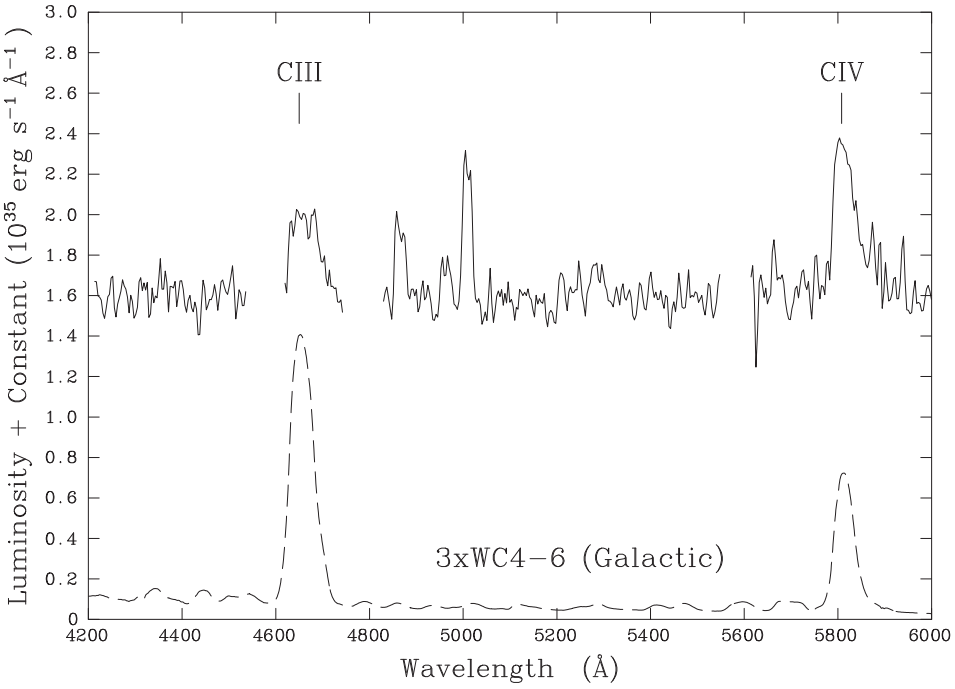

Figure D6. Spectrum of Source #49.

This paper has been typeset from a TEX/LATEX file prepared by the author.

Downloaded from https://academic.oup.com/mnras/article-abstract/473/1/148/4101236
by University of Central Lancashire user
on 02 November 2017